J Nanostruct 15(4): 1900-1915, Autumn 2025

RESEARCH PAPER

A FORC-Assisted Magnetic Hyperthermia Investigation of Fe_3O_4 Nanoparticles Synthesized at Different pH Values

Hashim Jabbar [1], Maan Al-Nuaim [2], Adil A. Al-Fregi [3], Zuhair Ali Abdulnabi [4]*

[1] *Department of Physics, College of Science, University of Basrah, Iraq*
[2] *Department of Pharmaceutical Chemistry, College of Pharmacy, University of Basrah, Iraq*
[3] *Department of Chemistry College of Science, University of Basrah, Iraq*
[4] *Department of Marine Chemistry, Marine Science Center, University of Basrah, Iraq*

ARTICLE INFO

Article History:
Received 02 June 2025
Accepted 26 September 2025
Published 01 October 2025

Keywords:
Co-precipitation
Fe_3O_4 nanoparticles
FORC diagram
Magnetic hyperthermia
pH value
Superparamagnetic behavior

ABSTRACT

Exploiting characteristics of magnetic nanoparticles (MNPs), especially superparamagnetic (SP) behavior, can lead to advancements in their possible practical applications such as hyperthermia therapy. Here, a facile co-precipitation method with different pH values is employed to synthesize Fe_3O_4 MNPs, followed by thoroughly characterizing them in terms of structural, morphological, magnetic, and calorimetric properties. According to X-ray and first-order reversal curve (FORC) analyses, all of the spinel Fe_3O_4 MNPs are found to show SP features. Hyperthermia measurements of ferrofluids acting as nanoheaters at a concentration of 8 mg/ml in a distilled water medium are carried out at a frequency of 400 kHz under different alternating magnetic field intensities. The maximum specific loss power (SLP) value and SP fraction are obtained to be 99 W/g and 50% using pH=12, respectively, resulting from a low hydrodynamic size distribution, high SP fraction and saturation magnetization, along with a considerably low coercive field of the MNPs.

How to cite this article
Jabbar H., Al-Nuaim M., Al-Fregi A., Abdulnabi Z. A FORC-Assisted Magnetic Hyperthermia Investigation of Fe_3O_4 Nanoparticles Synthesized at Different pH Values. J Nanostruct, 2025; 15(4):1900-1915. DOI: 10.22052/JNS.2025.04.037

INTRODUCTION

The treatment of cancer, as one of the most complicated diseases, is usually carried out with a combination of radiation therapy, chemotherapy and/or immunotherapy, in addition to surgical tumor resection. However, these methods are not risk-free since they can damage normal tissues, making the complete elimination of cancer doubtful [1,2]. Therefore, alternative therapies for cancer are becoming more and more popular, among which the thermal therapy with well-established benefits have attracted the attention of researchers. In fact, the degree and magnitude of the temperature increase involved in the thermal therapy can affect the treatment efficiency [3,4].

Applications of magnetic nanoparticles (MNPs) and fluids have recently become more widespread in the field of biomedicine [5]. Notably, magnetic resonance imaging, drug delivery, cell sorting, magnetic hyperthermia, and other research areas are considered potential applications of MNPs [6]. In the case of magnetic hyperthermia applications, a high-frequency alternating magnetic field (AMF) is used to treat tumor-loaded tissue via a magnetic fluid in an attempt to increase its temperature.

A perfect hyperthermia treatment would

* *Corresponding Author Email: hashim.jabbar@uobasrah.edu.iq*

target and kill only the tumor cells, so that the surrounding healthy tissue remains intact. The relevant temperature range (between 41 and 48 ºC) is known to be appropriate for hyperthermia treatments, involving multiple benefits and drawbacks [7, 8]. In fact, the attempt to find the specific loss power (SLP) or specific absorption rate i.e. the amount of energy absorbed per unit of MNP's mass, is a crucial first step in developing an effective hyperthermia treatment. The physical and chemical characteristics of the MNPs, including crystallinity, morphology (size and shape), saturation magnetization (Ms), and composition have significant impacts on the SLP parameter [9, 10].

Furthermore, the heating performance of MNPs is influenced by the interplay between particles and biological systems as well as by interparticle magnetic interactions [11,12]. The particles that have been used up to this point are either specifically engineered to bind to cancerous cells or are injected in situ into the tumor. Most studies have employed superparamagnetic (SP) magnetite (Fe_3O_4) or maghemite (γ-Fe_2O_3) MNPs in water-based suspensions due to their high biocompatibility and specific tumor targeting, low toxicity, and large Ms It should be noted that, the heat conduction away from the target area and blood perfusion surrounding the tumor make it difficult to have in vivo MNP concentrations that allow for adequate heating [13]. The undesirable heating caused by eddy currents in the nearby healthy tissue presents a second major obstacle [14-17].

Magnetite MNPs that meet nearly all clinical needs have been synthesized using a variety of precursors and techniques in order to study their magnetic hyperthermia properties [18]. In other words, considerable research has been performed with the aim of improving magnetic susceptibility of the MNPs in order to enhance their induction heating capability. In this regard, while some techniques such as modulating particle size [19-21], regulating composition [22–25], adjusting shape [26-29], and altering surface [30,31] have been introduced, their implementation may be difficult and cumbersome. Therefore, other approaches related to the synthesis parameters (such as solution temperature, pH, reaction time, precursor concentration, etc.) have been proposed to change physiochemical properties of the MNPs, while also enhancing their magnetic induction heating. Vayssières et al. showed that, by regulating the pH and the ionic strength imposed by a non-complexing salt in the precipitation medium, particle size can be tailored. The particle size decreases with increasing pH and ionic strength. Secondary particle growth by Ostwald ripening stops occurring above a critical pH value, which is determined by temperature and ionic strength [32]. The impact of the initial pH and temperature of iron salt solutions on the co-precipitation formation of Fe_3O_4 MNPs was documented by G. Gnanaprakash et al. [33]. Their findings demonstrate that crucial factors influencing the size and composition of the synthesized MNPs are the initial pH and temperature of the ferrous and ferric salt solution prior to the start of the precipitation reaction. Moreover, smaller particles have higher SLP than larger ones [33].

Ramadan et al. [34] synthesized Fe_3O_4 MNPs using a co-precipitation aqueous method at room temperature and at varying pH values, ranging from 8 to 12.5. It was discovered that the pH level had no noticeable impact on the particle size, but had a major effect on the phases of Fe_3O_4 MNPs. Magnetite was determined to be the predominant phase in each instance, but the goethite phase's contribution was readily discernible as the pH rose. There was a significant drop in saturation magnetization [32]. Myrovali et al. [35] adjusted the solution's pH levels (9.0–13.5) using an aqueous precipitation method, yielding a broad range of average MNP diameters from 16 to 76 nm. They demonstrated how each MNP size and combination of parameters relating to the various heat generation mechanisms (Brownian, Néel, and hysteresis losses) determined the maximum heating efficiency [33].

The aim of this work is to use a facile co-precipitation method with different pH values in order to synthesize Fe_3O_4 MNPs in an air atmosphere without the need for a surfactant. The effects of pH values on the sizes, geometries, and ultimately the magnetic properties of Fe_3O_4 MNPs are the main focus of this study. Additionally, the control of pH on the superparamagnetic fraction is investigated, allowing for the modification of the functionality of Fe_3O_4 MNPs in applications involving hyperthermia.

MATERIALS AND METHODS

Materials

Ferric chloride hexahydrate ($FeCl_3.6H_2O$) and

ferrous chloride hexahydrate ($FeCl_2.6H_2O$) were purchased from Merck (Germany) and Bendosen (Malaysia) companies, respectively. Ammonium hydroxide (NH_4OH, 32%, Merck) and ethanol (C_2H_5OH, R&M Chemicals) were also purchased.

Synthesis of Fe_3O_4 MNPs

A co-precipitation method was utilized to synthesize Fe_3O_4 MNPs. To this end, two 100-ml beakers of deionized water were initially filled with separate stoichiometric solutions of $FeCl_2.6H_2O$ and $FeCl_3.6H_2O$, and then continuously stirred at room temperature. Once both solutions had completely dissolved, they were filtered 3 times (see Fig. S1 in Supplementary Material). The precursor solutions were gradually poured into a beaker containing 1200 ml of deionized water, with Fe^{2+}/ Fe^{3+} molar ratio being constant to 2/3 for different samples. NH_4OH was also added dropwise in order to prepare the final solution with pH= 10.0 (sample S1), 11.0 (sample S2) and 12.0 (sample S3), according to Fig. S2 in Supplementary Material. After 30 min of vigorous stirring, the solution color darkened, indicating the formation of black precipitates. These precipitates were allowed to settle down using a large magnet, followed by separating the supernatants. To eliminate the unreacted precursors, pure water was used to wash the black precipitates continually until the pH of the solution reached 7.0 ± 0.2. Finally, the

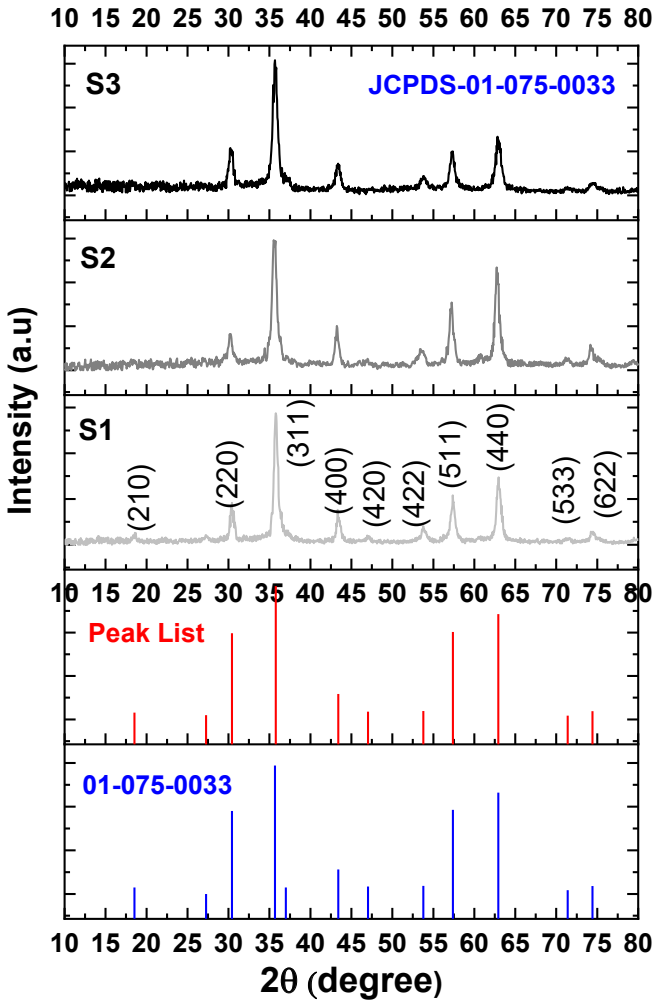

Fig. 1. (Top 3 panels) XRD patterns of Fe_3O_4 MNP samples S1, S2 and S3. (Bottom 2 panels) Peaks list (red) of sample S1 matched with the JCPDS reference card (blue).

samples were cleaned with ethanol and left to air dry at room temperature for one day.

Characterization

Following the synthesis of the Fe_3O_4 MNP samples, X-ray diffraction (XRD; Philips, X'Pert Pro; Cu Kα radiation with λ = 0.154 nm) analysis was employed to examine their crystal structure and crystallite size. Additionally, field-emission scanning electron microscopy (FESEM; MIRA3 TESCAN) along with energy dispersive spectroscopy (EDS) was used to investigate the morphology of MNPs, and their mean diameter and elemental composition.

By using a Spectrum BX spectrometer (Perkin Elmer) in the transmission mode (4 cm^{-1} in resolution), Fourier transform infrared (FTIR) spectra of finely ground MNP samples were distributed throughout KBr pellets and recorded. To ascertain the size distribution of MNPs in the aqueous solution or suspension, dynamic light scattering (DLS; Horiba Jobin Yvon) analysis was utilized. The functional groups of the active compounds were identified using FTIR spectroscopy within the infrared radiation region (4000-500 cm^{-1}) in order to verify the chemical state and successful synthesis of Fe_3O_4 MNPs at different pH values.

A vibrating sample magnetometer (VSM; MDK) was used to measure hysteresis loops in order to examine magnetic characteristics of MNPs at ambient temperature. Furthermore, FORC analysis was carried out to assess the hysteresis loop results and provide further information on the magnetic properties. The following is the process used to carry out the FORC analysis: Initially, the MNP sample was positively saturated with a maximum magnetic field (H_{max}). This field was then reduced to a reversal field H_r ($H_r < H_{max}$) with certain steps to obtain FORCs (see Figs. S3 and S4 in Supplementary Material). On the other hand, hyperthermia measurements were performed using a hyperthermia system (MDK). More details on the instrumentation and experimental procedures are presented in Supplementary Material.

RESULTS AND DISCUSSION

Crystal structure, chemical state, and morphology

The crystal structure, crystallite size, and crystalline phase of dried Fe_3O_4 MNP samples were examined by XRD analysis, and the results are displayed in Fig 1. The crystalline phase of the MNPs possesses prominent diffraction peaks at 2θ= 18.5º, 27.2º, 30.4º, 35.6º, 43.4º, 47.02º, 53.7º, 57.4º, 62.9º, 71.4º and 74.4º, which can be indexed as (210), (220), (311), (400), (420), (422), (511), (440), (533), and (622) planes, respectively. The narrow and well-defined diffraction peaks indicate the high crystallinity of the samples, regardless of the pH value. By comparing the XRD patterns with the cubic spinel structure of Fe_3O_4 (JCPDS card no. 01-075-0033) in terms of diffraction positions and intensities, the formation of Fe_3O_4 MNPs with spinel structure is confirmed for samples S1, S2, and S3 [36]. Moreover, no additional peaks related to impurities or secondary phases such as Fe_2O_3 are observed in the XRD patterns of the MNPs synthesized at different pH values.

Table 1 presents the *d*-spacing (i.e., the crystalline lattice plane distance) experimentally obtained from the XRD analysis, and the *d*-value (calculated theoretically based on the reference card) for sample S1. Meanwhile, Table 2 the average crystallite size (d_{XRD}) of the three samples estimated for the main peak (i.e., (311)). The Scherrer equation was used to estimate these sizes:

$$d_{XRD} = \frac{0.9\lambda}{\beta \cos\theta} \quad (1)$$

where θ is the Bragg diffraction angle (half of 2θ), β (in radians) denotes FWHM, and λ is the X-ray wavelength with Cu Kα radiation. It is clear from the comparison between the peak intensities of the three samples–particularly the main peak (311)–that the crystallinity increases with increasing the pH value to 12. It is also observed that the crystallite size of the MNPs given in Table 2 decreases slightly with increasing pH.

The FTIR spectra obtained from the Fe_3O_4 MNP samples are shown in Fig. 2. These spectra show absorption peaks in the range of 3170- 3345 cm^{-1}, which can be associated with the (-OH) group. The stretching and bending vibrations of the OH group absorbed from water molecules (O-H) on the surface of Fe_3O_4 MNPs are responsible for the peaks around 3372 and1620 cm^{-1}, respectively [37].

The energy absorbed around550 cm^{-1} (Fig. 2) is assigned to the vibration of metal oxide (M-O), especially the Fe-O bond of iron oxide [37, 38]. All

of the Fe_3O_4 MNP samples synthesized by varying pH conditions, S1 (pH =10), S2 (pH =11) and S3 (pH =12), display significant vibrational bands at some positions, particularly in the spinel Fe_3O_4 fingerprint, according to their FTIR spectra. Due to O-H stretching, samples S1, S2, and S3 show broad strong bands at 3372, 3345 and 3170 cm^{-1}, respectively. Similarly, the strong bands at 1623,1619 and 1620 cm^{-1} are attributable to O-H stretching for samples S1, S2, and S3, respectively. These bands are responsible for protonating some metal-oxygen bonds, converting them into hydroxyl groups. An increase in the degree of hydroxyl groups is induced by the bands, thus becoming more intense and shifting toward a higher frequency when decreasing the pH value.

Fig. 3 shows FESEM images of Fe_3O_4 MNP samples synthesized by the co-precipitation

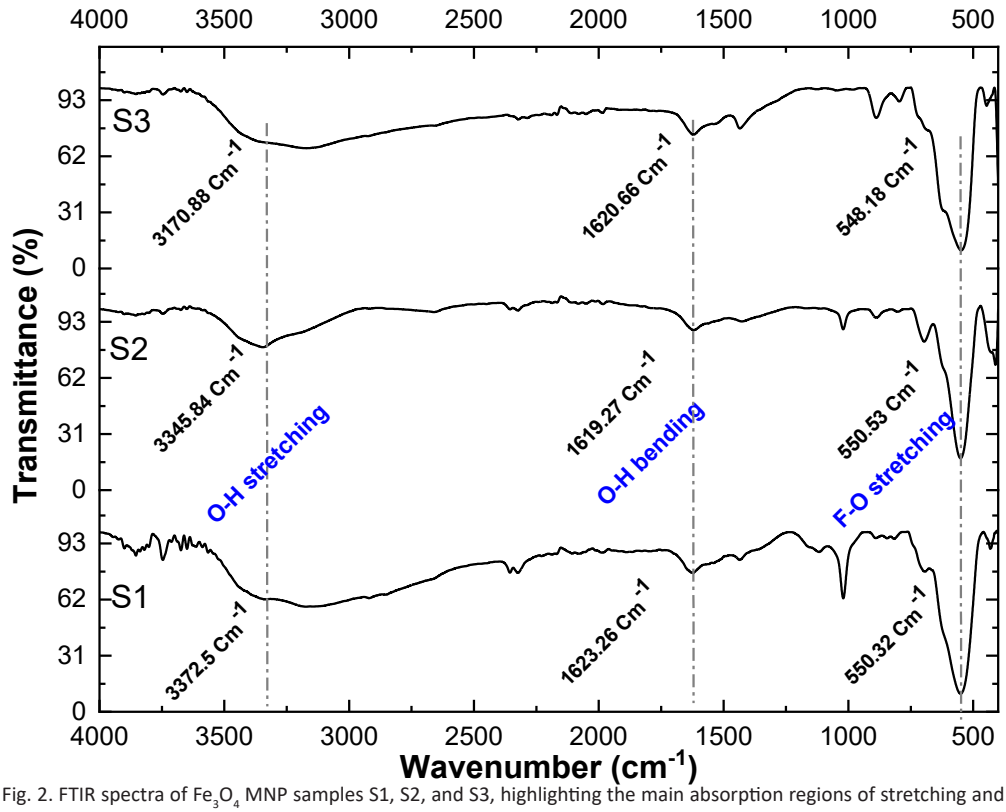

Fig. 2. FTIR spectra of Fe_3O_4 MNP samples S1, S2, and S3, highlighting the main absorption regions of stretching and bending vibrations.

Table 1. The interplanar distance values extracted from XRD analysis of sample S1 and theoretical calculations.

2θ (degree)	(hkl)	d-spacing (XRD) (Å)	d-value (Ref. card) (Å)	Relative error
30.4198	(220)	2.94868	2.9380	0.00363
35.7768	(311)	2.50899	2.5080	0.00039
43.4064	(400)	2.07923	2.0775	0.00054
53.7803	(422)	1.70644	1.6962	0.00603
57.3885	(511)	1.60338	1.5992	0.00261

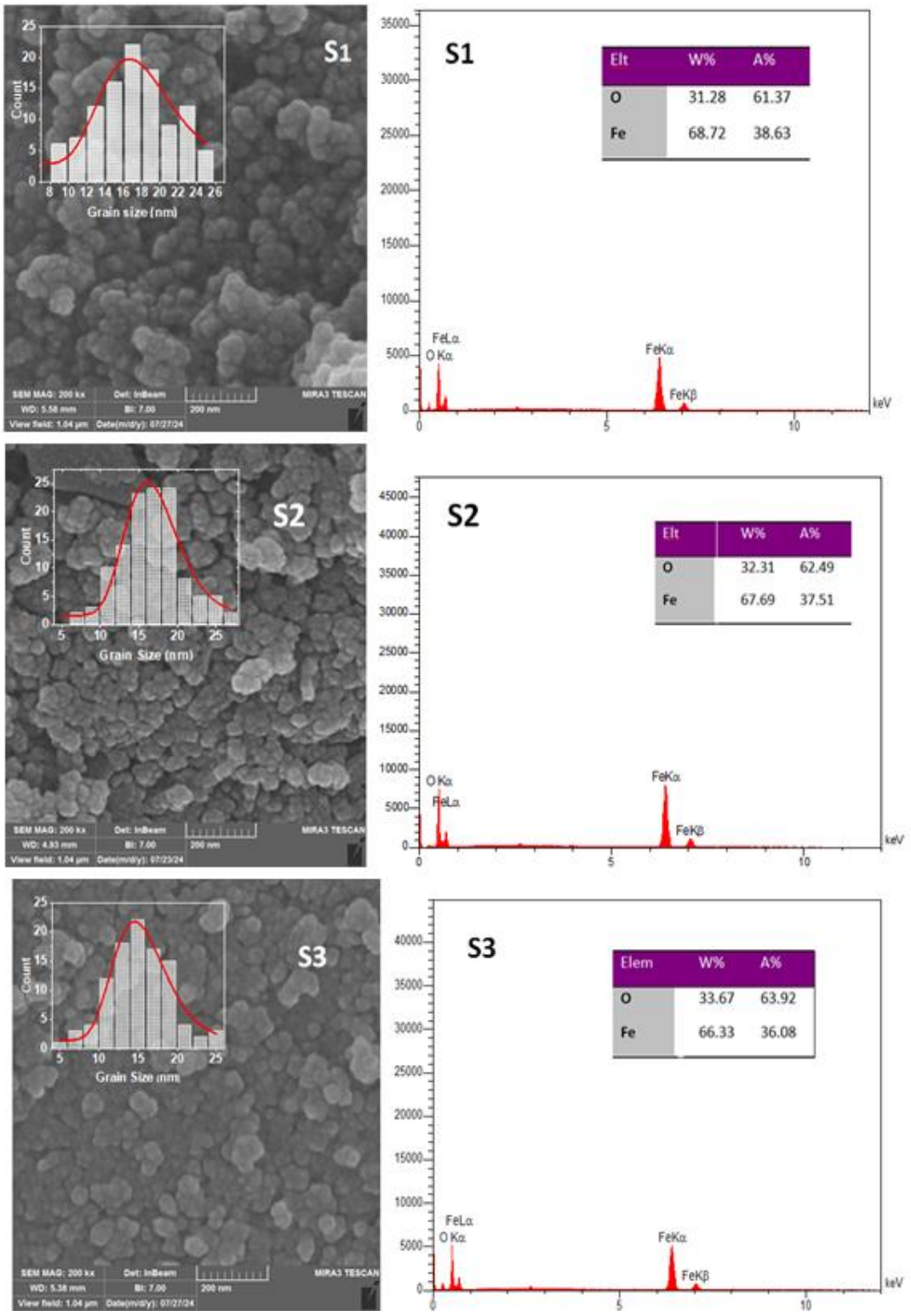

Fig. 3. FESEM images and EDS spectra of Fe_3O_4 MNP samples , and . TheMNP grain size distribution histograms are represented by the top-left insets in the FESEM images. The corresponding elemental analysis is presented in the insets of EDS spectra.

method at different pH values, along with the corresponding size distribution histograms and EDS spectra. It is found that the morphology of MNPs is almost spherical.

To obtain a statistically accurate interpretation of the data, the image analysis program Image-J was used, allowing for the estimation of the diameters of many particles from the displayed micrographs, and plotting the size distribution histograms included in each image. A log-normal function was used to fit the histograms (the continuous red line) for each size distribution. The distribution mean and standard deviation σ were then computed. A maximum number of particles must be chosen as part of the sample preparation process in order to balance the desired accuracy with the performance required to achieve it. The number of particles used for the calculations ranged between 100–200 particles.

The size distribution histograms also demonstrate the expected rise in MNP grain size with decreasing pH. The values of the grain size are presented in Table 2. The fact that d_{XRD} is less than the grain size for each sample suggests that the Fe_3O_4 MNPs are polycrystalline in nature. Furthermore, the lack of the use of surfactant during the synthesis process may be the cause of the size distribution of the MNPs. Surfactants can stabilize NPs by minimizing inter-particle interactions and encasing them in a protective coating. By sticking to the surface of NPs, surfactants create a barrier that prevents agglomeration. As a result, adding surfactants to MNPs preserves their magnetic characteristics and functionality, while also enhancing their stability and dispersion [39].

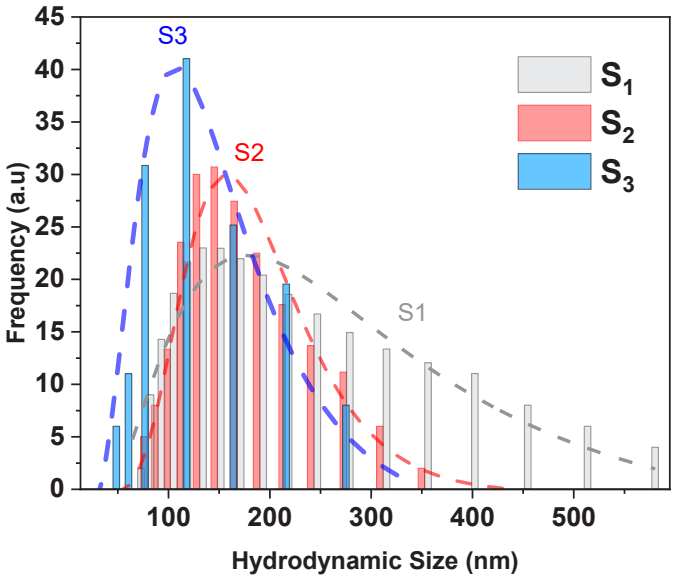

Fig. 4. DLS particle size distributions for Fe_3O_4 MNP samples (grey), (red), and (blue). A log-normal function was used to fit the size distributions of the three samples.

Table 2. Statistical parameters of crystallite size () and grain size and of the synthesized Fe_3O_4 MNP samples calculated based on XRD patterns and FESEM micrographs.

MNP Sample	d_{XRD} (nm)	Grain size (nm)	standard error of size
S1	7.92	16.74	0.0474
S2	7.75	15.85	0.0453
S3	7.53	14.89	0.0447

The size distribution of the MNPs with quasi-spherical shape is narrow, leading to grain size values in the range of around 14-16 nm, according to the fits by a log-normal distribution function. As can be concluded, the size of Fe_3O_4 MNP samples synthesized by changing pH conditions, S1 (pH =10), S2 (pH =11) and S3 (pH =12), is reduced. The histograms (insets of Fig. 3) were obtained by statistical analysis of FESEM images of the Fe_3O_4 MNPs using ImageJ software.

Hydrodynamic MNP size distribution

DLS analysis was employed to explore the size distribution of the MNPs in the aqueous solution. The idea of Brownian motion, which holds that particles move randomly in a liquid or gas medium, provides the foundation for the DLS concept. The primary advantage of DLS method

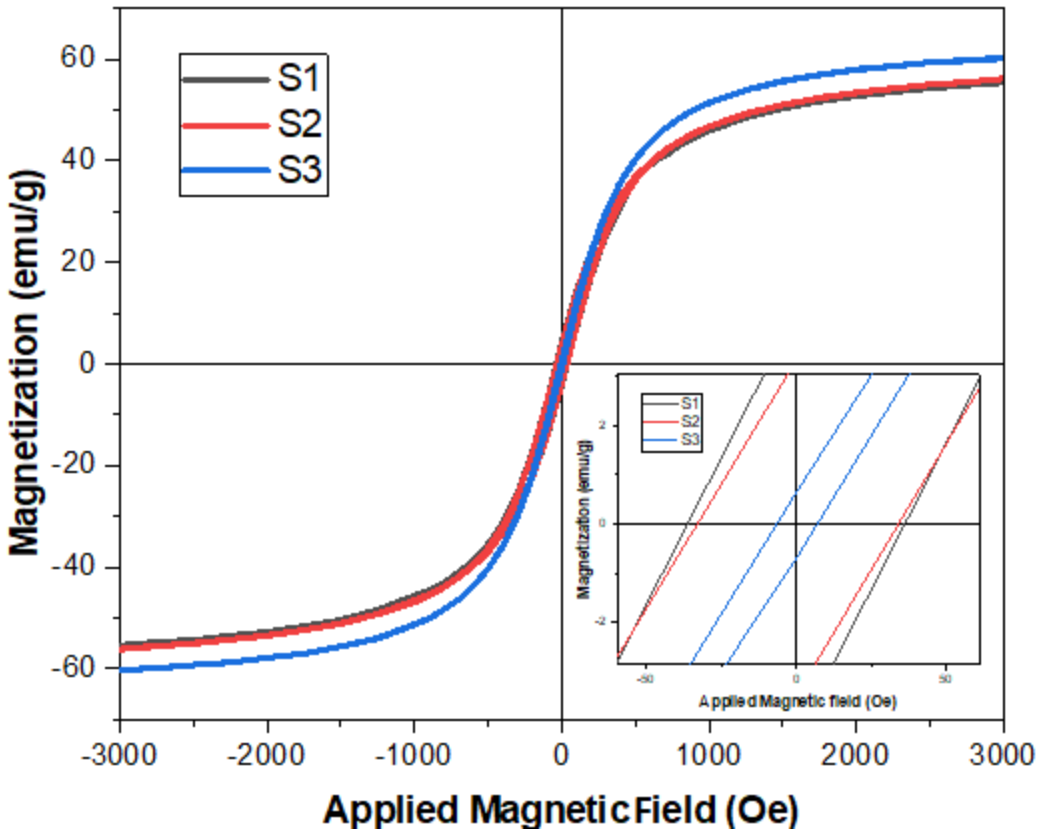

Fig. 5. Hysteresis loops of Fe_3O_4 MNP samples measured at room temperature. The bottom-right inset magnifies the hysteresis loops at a lower magnetic field range.

Table 3. Mean hydrodynamic size (derived from a log-normal fit) and polydispersity index values of Fe_3O_4 MNP samples.

MNP sample	Hydrodynamic size (nm)	Polydispersity index	Standard error of size
S1	198.24	0.473	0.0249
S2	177.06	0.404	0.0187
S3	121.28	0.386	0.0146

over other particle size measurement techniques is its ability to examine particle size distributions at the nanoscale.

As a crucial factor for the possible use in biomedical applications, the stability of MNPs was evaluated in solution. Fig. 4 displays hydrodynamic size distributions obtained from the DLS analysis. Meanwhile, Table 3 presents mean hydrodynamic size and polydispersity index values of the MNP samples. Generally, while DLS may be used to describe the hydrodynamic behavior or size of organized aggregates of NPs, it cannot distinguish their different compositions. By considering Tables 2 and 3, the aggregate sizes obtained from the FESEM images deviate from the DLS hydrodynamic sizes (being in the range of around (121-198 nm). Nevertheless, the hydrodynamic size of the MNP aggregates is reduced with increasing pH, being in agreement with the decreasing trend of mean diameter observed in the FESEM images. Also, the hydrodynamic size of the MNP aggregates varies from sample to sample, and the corresponding polydispersity index values indicate that the width of the size distribution is not uniform across the samples.

Magnetic characteristics

Magnetic characteristics of MNP samples were examined at room temperature using hysteresis loops measured by applying a magnetic field of 3kOe. The hysteresis loops of the MNPs synthesized at different pH values are displayed in Fig. 5. The quantitative results extracted from the hysteresis loop measurements, including M_s, remanence magnetization (M_r), and coercivity (H_C) are presented in Table 4.

As can be seen, M_s values of samples S1, S2 and S3 are 55.43, 56.27 and 60.32 emu/g, respectively. Therefore, sample S3 synthesized at pH= 12 has the maximum M_s value, which is less than M_s of bulk iron oxide materials (~ 90 emu/g) [40]. On the other hand, H_C values of samples S1, S2 and S3 are found to be 36.2, 32.9 and 6.7 Oe, respectively. In this case, H_C value of sample S3 is minimum, being considerably lower than that of samples S1 and S2. This reduction in H_C may occur due to the higher contribution of SP Fe_3O_4 MNPs, affecting the overall magnetic properties.

A closer look of the initial VSM magnetization results reveals that, as the size of the particles decreases, Ms increases and H_C decreases. The

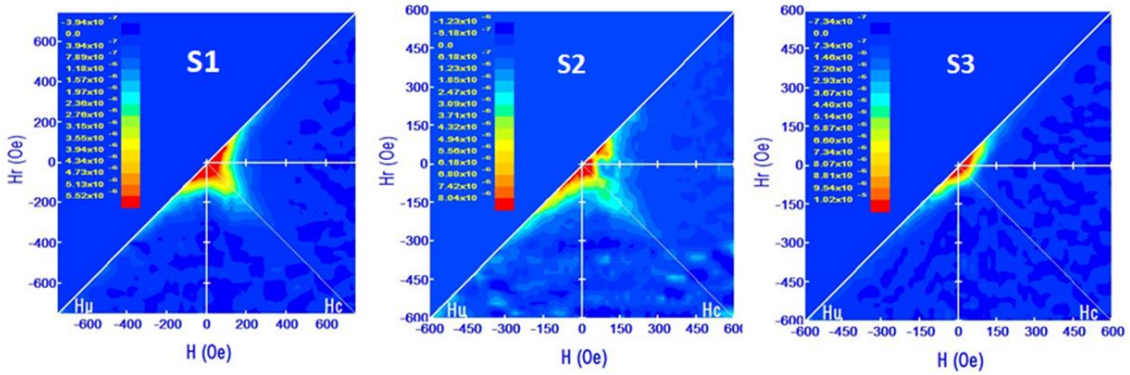

Fig. 6. Two-dimensional FORC diagrams of Fe_3O_4 MNP samples (S1, S2 and S3) measured at room temperature.

Table 4. Magnetic parameters of MNP samples extracted from hysteresisloop and FORC measurements.

MNP sample	Ms(emu/g)	Mr(emu/g)	Hc(Oe)	SP fraction (%)
S1	55.43	4.308	36.2	11
S2	56.27	3.334	32.9	20
S3	60.32	0.643	6.7	50

sizes of Fe_3O_4 MNPs falling within the critical boundary of a SP–ferrimagnetic transition might be the cause of these results. However, the magnetic properties such as M_s and H_C are somehow not determined by size. According to some studies, the SP–ferrimagnetic transition in Fe_3O_4 MNPs takes place at around 20 nm [41] or even around 30 nm [42]. The single-domain (SD) to multidomain (MD) transition depends on the overall size, degree of crystallinity, and surface characteristics of NPs, and occurs at varying values, much like the SP–ferrimagnetic transition. Due to a number of contributing factors, it is therefore difficult to predict the relationship between the size and magnetic properties of Fe_3O_4 NPs. The size and shape of the NPs have a significant impact on these variables, which are also correlated with one another. Finite size effects are usually associated with unique behaviors of a material at a finite nanoscale size, involving electron quantum confinement [43]. The most researched finite size effects in nanomagnetism are the SD limit and the SP limit, which generally determine the magnetic behavior of particles for ferrimagnetic and SP responses, respectively [43].

Regarding hyperthermia applications, there are three independent mechanisms, including Brownian relaxation, hysteresis loss, and Néel relaxation, which contribute to producing thermal energy in response to stimulation. The relative contribution of each is strongly dependent on size, shape, magnetocrystalline anisotropy, and degree of agglomeration of the NP. The SD NPS have been demonstrated to absorb considerably more energy at physiologically relevant magnetic fields and frequencies than MD particles [44]. It is unquestionably true that magnetic particles larger than 100 nm experience heating caused by shifting domain walls [45]. Hysteresis loss is still important for larger SD particles, but for smaller particles, H_C and M_r bruptly disappear and are highly dependent on particle volume [46]. Specifically, coercivity can be expressed as follows: $H_C = (2K/MS)[(1-(V_C/V)^{(1/2)}]$ for $V>V_C$, where V_C is the critical volume of particle, below which relaxation effects predominate [12]. This dominance happens when the particle's relaxation time equals the field frequency ($\omega\tau=1$).

The hysteresis loop results were assessed using FORC analysis, thereby allowing for a closer examination of the magnetic properties. In actuality, the coercive and interaction field distributions are revealed by FORC measurements, which record the magnetic fingerprints of materials [47,48]. The samples used for the FORC measurements were ground into a powder and then immobilized by pressing them firmly into gel caps. At room temperature, FORCs were conducted using a VSM device (MDK) equipped with FORC software, as shown in Fig. S3 of Supplementary Material.

Prior to tracing 50 magnetization curves $M(H_r, H)$ at a reversal field (H_r) from the major hysteresis loop M(H), with H serving as the measurement point along the loop, the sample was first saturated with a positive applied field of 600–700 Oe. The field increment and average measurement time were 20 O.

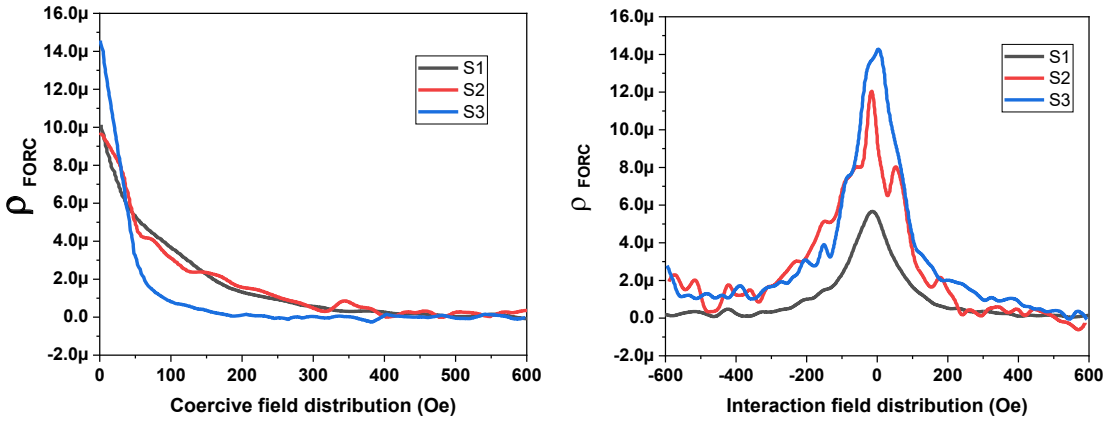

Fig. 7. The left panel represents the coercive field distributions, and the right panel represents interaction field distributions of Fe_3O_4 MNP samples.

$$\rho(H, H_r) = -\frac{1}{2}\frac{\partial^2 M(H, H_r)}{\partial H\, \partial H_r} \quad (2)$$

The H_C and H_u axes are defined by the following relations:

$$H_C = \frac{H - H_r}{2},\ H_u = \frac{H + H_r}{2} \quad (3)$$

It is possible to switch the coordinate system from {H, H_r} to {H_C, H_u}, where H_C and H_u represent the coercive field and interaction field, respectively. A contour plot of the FORC distribution, with H_C on the horizontal and H_u on the vertical axes, is called a FORC diagram. In the first approximation, the vertical axis (H_u) of the FORC diagram shows information about the magnetic interaction between particles, whereas the horizontal axis, which represents the coercive field (H_C), is sensitive to grain size and composition [47,48]. A smoothing factor of two was used when processing all FORC diagrams.

Fig. 6 displays FORC diagrams of Fe_3O_4 MNP samples (S1, S2 and S3), and the corresponding coercive and interaction field distributions are depicted in Fig. 7. As observed, FORC distributions are dominantly positioned near the origin of the diagrams (i.e., H_C= 0 Oe and Hu= 0 Oe), indicating SP the behavior of the Fe_3O_4 MNPs synthesized at different pH values. In the case of pH= 12 (sample S3), the FORC distribution is more concentrated around the origin, revealing the higher formation of the SP MNPs. In turn, this confirms the hysteresis loop results (having the maximum and minimum values of M_s and H_C, respectively) obtained for sample S3.

Noticeably, the FORC distributions of samples S1 and S2 are partly broadened along the H_C axis, which can be considered the reasoning behind their higher H_C values (36.2 and 32.9 Oe) compared to sample S3 (6.7 Oe). In addition, the FORC distribution of the samples is broadened along H_u axis, representing the magnetic interactions. In fact, since the reversible magnetization is present, the ρ distribution along a profile where H_C=0 Oe, is referred to as a reversible ridge, being linked to low-coercivity rotating particles. The reversible ridge in samples S1 and S3 is relatively symmetrical, having a FORC distribution along H_u=0 Oe. The spread in the interaction field distribution along the H_u axis becomes more broadened with decreasing coercivity, involving the effect of collective non-coupled reversible magnetization due to the existence of the SP phase. The majority of the SP phase of the sample S3 contributes to the positive interactions of a magnetizing nature, being more prevalent within it, as inferred from the FORC distribution analysis.

The reason for the lack of symmetry in the FORC distribution of sample S2 along the H_u axis might be due to the small portion of MNPs with reversible magnetization coupled to both the system's irreversible state and the applied field. The distribution peak for the sample with the finest grain size nearly overlaps with a SD-like peak. Pseudo-single domain (PSD) grains have been reported to have a combination of multidomain (MD)-like moments with both closed SD-like and diverging contours [48, 49]. Accordingly, sample S2 which is primarily composed of SD particles has the greatest coercive field distribution. The lower H_C of this sample compared to sample S1 can be justified by a higher contribution of SP MNPs.

Deconvolution of both reversible and irreversible components is possible using FORC analysis. The irreversible component originates from the magnetically blocked particles, whereas the reversible component is contributed by SP particles and the reversal magnetization of SD particles. The reversible contribution for non-interacting SD particles with uniaxial magnetocrystalline anisotropy is expected to be 50%. In principle, FORC analysis estimates the SP fraction by deducting the irreversible fraction of magnetization from the reversible fraction, keeping in mind that the total of the two fractions will be 1 or 100% (see Fig. S5 in Supplementary Material). In this regard, SP fractions of Fe_3O_4 MNP samples (S1, S2 and S3) estimated from the FORC analysis are presented in Table 4. As expected from its minimum grain size and H_C value, sample S3 has the maximum SP fraction (50%), making it a potential candidate for hyperthermia applications. Moreover, sample S2 has a higher SP fraction (20%) compared to sample S1 (11%).

Magnetic hyperthermia evaluation

To determine a quantitative evaluation of the heating efficiency of the Fe_3O_4 MNPs, thermometric measurements were carried out. In this regard, ferrofluids containing Fe_3O_4 MNPs were prepared in glass test tubes and located in a Teflon holder for the hyperthermia measurements.

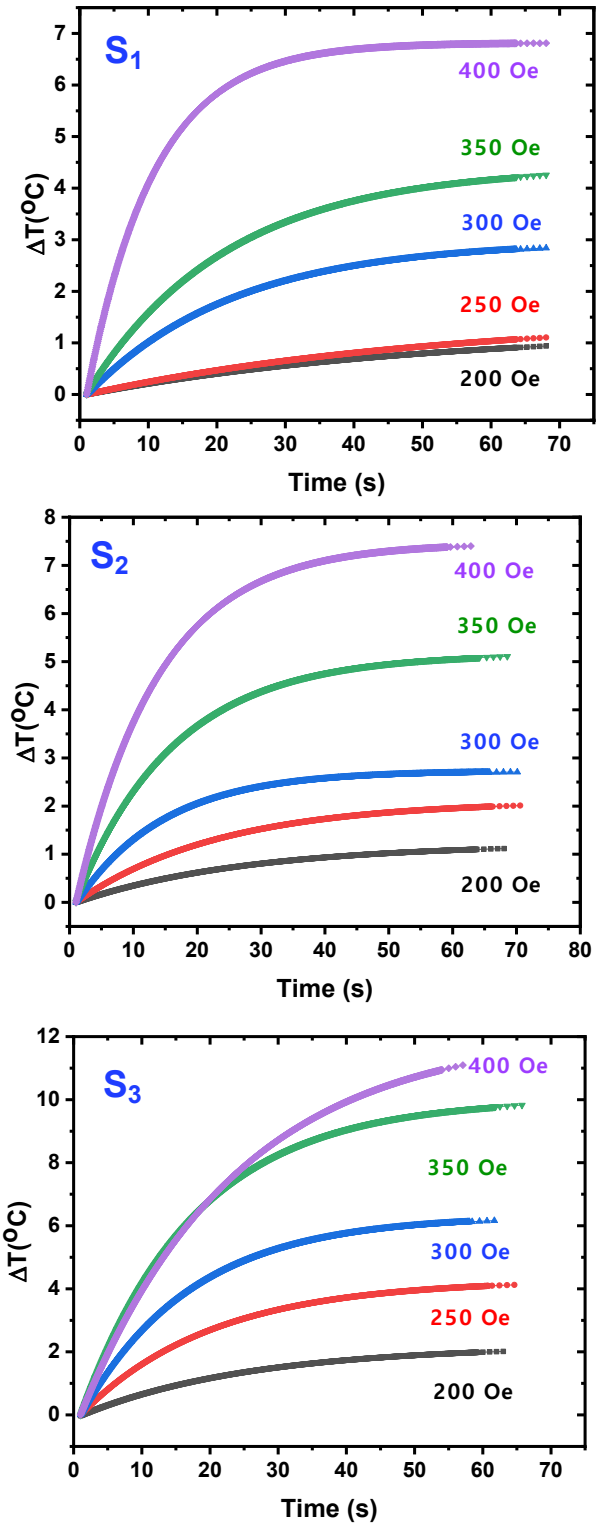

Fig. 8. Thermal responses of the ferrofluids of MNP samples , , and with a concentration of 8 mg/ml in a water medium. The frequency is kept constant at , whereas the magnetic field intensity varies between 200–400 Oe.

The thermal curves were acquired after subjecting the ferrofluids to an AC magnetic field with f = 400 kHz and alternating magnetic field intensities in the range of H= 200–400 Oe for 60 s. To maintain good stability and avoid agglomeration of MNPs during the measurements, the ferrofluids with an MNP concentration of 8 mg/ml in a water medium were sonicated for 15 min, as shown exemplary involving heating-cooling transients (Figs. S8 and S9 in Supplementary Material). A calorimetric method was used to determine SLP via magnetic hyperthermia measurements (see Figs. S6 and S7 in Supplementary Material).

Fig. 7 shows T-t curves of MNP samples S1, S2, and S3 for H=200–400 Oe at f =400 kHz. The following formula was used to calculate the dissipated heat (SLP in terms of W/g) [50,51]:

$$\mathrm{SLP} = \mathrm{C_S}\left(\frac{\Delta T}{\Delta t}\right)\frac{\mathrm{M_{Sol}}}{\mathrm{M_{MNPs}}} \quad (4)$$

where ΔT/Δt represents the initial slope of the temperature-time curve, Cs is the specific heat capacity of the solvent (C_{Water}= 4.187 J/g°C), and M_Sol and M_MNPs are the masses of the solvent and MNPs, respectively. As illustrated in Fig. 8, at a given frequency (f = 400 kHz), the thermal response of all samples increases with increasing *H*. Alphandéry et al. proposed that, when the applied magnetic field intensity is nearly quadrupled, the corresponding SLP value increases almost eightfold, indicating the necessity of measuring SLP values under the same circumstances (f and H) as those used in magnetic hyperthermia therapy [52]. The effectiveness of MNPs in producing thermal energy from the applied electromagnetic energy is depicted in Fig. 9. Evidently, SLP value of all samples is maximized when f=400 kHz and H=400 Oe. Notably, sample S3 experiences the largest temperature rise (ΔT ~ 12 °C), leading to a maximum SLP value of ~99 W/g. Also, sample S2 shows a temperature rise of ΔT ~8 °C resulting in SLP~65 W/g . The lowest temperature rise (ΔT ~ 7 °C) or the minimum SLP value (~60 W/g) is obtained for sample S1.

The overall trend of all measurements shows that in maximum value of f = 400K Hz, there is a rise in the thermal response, which in turn leads to maximum SLP value. Soetaert et al. found a linear relationship between SLP and AMF frequency, so that an increase in f resulted in a higher SLP value [53]. It is noteworthy that the SLP values shown in Fig. 9 are different for the samples, being consistent with their FESEM and DLS results, which underlie the dependence of heat production mechanisms on magnetic characteristics and size effect of Fe_3O_4 MNPs. For ferro- and ferrimagnetic NPs, the hysteresis loss mechanism controls the heat generation mechanism, whereas the primary heating mechanisms for SP NPs are Néel and Brown relaxations [54]. According to magnetic property studies, 19 nm nanocubes are situated at the SP to ferrimagnetic transition point, which is in line with the theory put forth in earlier research regarding the higher SLP value of Fe_3O_4 MNPs in this transition size range [55]. According to Muro-Cruces et al., the best heating efficiency of Fe_3O_4 nanocubes with sizes of 13, 15, and 19 and 22 nm at H= 17 kA/m and f= 183 kHz was found for 19 nm cubic nanocrystals. The frequency and amplitude of the applied AC magnetic field have a notable impact on the heating efficiency of Fe_3O_4 MNPs. Myrovali et al. demonstrated that, for spherical MNPs, the highest SLP values were recorded in the size range of 16-37 nm. Since the inter-particle dipolar interaction rapidly diminished with distance, MNPs in this range were more isolated from one another at low concentrations.

Because of internal friction between the rotating magnetization and the crystal lattice in MNPs exhibiting SP behavior, Néel relaxation predominates the heating mechanism. Meanwhile, due to the friction between the rotating MNPs and the surrounding medium, Brownian relaxation is activated when the MNP size increases from the SP to the ferromagnetic SD size regime [35]. By fixing the magnetic moments with respect to the crystal orientation, the MNPs can rotate in the ferrofluid, while also involving the hysteresis loss contribution for larger MNPs.

In fact, ferrofluids containing MNPs with large Ms, high SP fraction, and low Hc typically exhibit increased stability and a relatively high SLP value [58]. This is due to strong reactions between MNPs under the AMF during the magnetization, demagnetization, and reversal magnetization processes caused by high Ms, thereby converting more electromagnetic energy into heat. On the other hand, low H_C not only makes Néel and Brownian relaxation mechanisms easier to contribute, but it also makes MNPs lose their magnetization when the magnetic field is removed, being a prerequisite for clinical treatment. The SLP of sample S3 is maximum, having a significantly

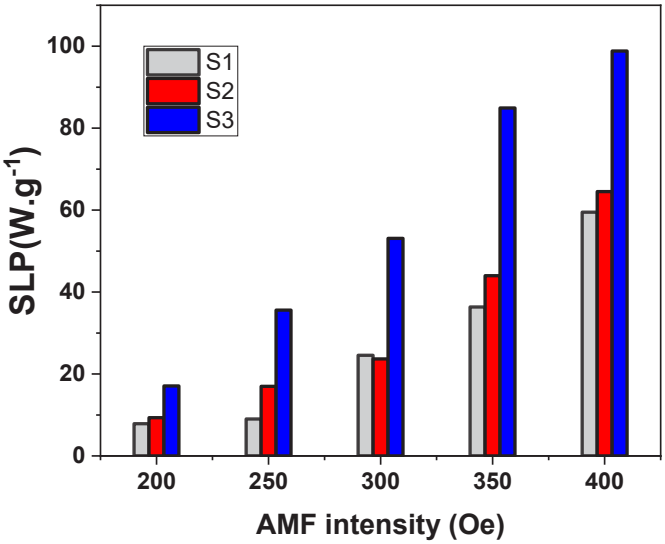

Fig. 9. SLP dependence on the magnetic field intensity and the frequency were set to for MNP samples S1, S2, and S3 with a concentration of 8 mg/ml in a water medium.

lower H_C and a higher Ms compared to H_C and Ms of samples S1 and S2. In other words, the significantly low Hc and relatively high Ms of sample S3 offer a good balance between these two magnetic parameters, ultimately resulting in the maximum SLP value of ~99 W/g.

Examining the heating performance of the different samples reveals that the SP contribution estimated by the FORC measurements has a significant influence on the of (ΔT/Δt) value. In fact, sample S3 with the highest SP fraction (50%) results in the maximum SLP, indicating the highest contributions of Néel and Brownian relaxation mechanisms to the heating efficiency. Moreover, samples S1 and S2 have more contributions of SD MNPs, thus producing heat via the hysteresis loss mechanism. Therefore, samples S1 and S2 exhibit an enhanced hysteresis loss mechanism, whereas the heat generation of sample S3 is primarily attributed to Néel and Brownian relaxation mechanisms. Accordingly, the maximum SLP obtained from sample S3 is mainly achieved through a balanced combination of Néel and Brownian relaxations, as well as the hysteresis loss mechanism.

CONCLUSION

In conclusion, Fe_3O_4 MNPs have been synthesized at pH values of 10,11, and 12 through the use of the straightforward and affordable chemical co-precipitation technique. The pure magnetite nature of the MNPs with inverse spinel structure was confirmed by the XRD and FTIR analyses. The FESEM images showed the formation of nearly spherical MNPs, whose mean diameters were 16.74, 15.85, and 14.89 nm for pH values of 10,11, and 12, respectively. DLS particle size distributions revealed a reduction in the polydispersity with increasing the pH value. The hysteresis loop results demonstrated a significant reduction in H_C value (6.7 Oe) of the MNPs with Ms of 60.32 emu/g synthesized at pH= 12, indicating their SP behavior. Additionally, the FORC analysis confirmed the hysteresis loop results, estimating that the SP fraction varied from 11% (pH= 10) to 20% (pH= 11) and 50% (pH= 12). The ferrofluid containing Fe_3O_4 MNPs (pH= 12) dispersed in a distilled water medium with a concentration of 8 mg/ml resulted in the highest temperature rise (ΔT=12 °C) under the AMF (H_{max}=400 Oe), giving rise to the maximum SLP value (99 W/g). The MNPs generated the maximum amount of heat due to a balanced combination of the high Ms and low H_C, involving Néel and Brownian relaxations, as well as a hysteresis loss mechanism. The lowest temperature rise (ΔT ~ 7 °C) was obtained for the ferrofluid consisting of the MNPs synthesized at pH= 10, resulting in the minimum SLP value (~60

W/g). Therefore, the pH used in the chemical synthesis of MNPs can be considered an influential parameter in adjusting magnetic hyperthermia properties.

ACKNOWLEDGEMENTS

The authors would like to thank MDK Company's team and Department of Physics in University of Kashan for their kind assistance.

CONFLICT OF INTEREST

The authors declare that there is no conflict of interests regarding the publication of this manuscript.

REFERENCES

1. Datta NR, Rogers S, Ordóñez SG, Puric E, Bodis S. Hyperthermia and radiotherapy in the management of head and neck cancers: A systematic review and meta-analysis. International Journal of Hyperthermia. 2015;32(1):31-40.
2. Issels RD, Lindner LH, Verweij J, Wust P, Reichardt P, Schem B-C, et al. Neo-adjuvant chemotherapy alone or with regional hyperthermia for localised high-risk soft-tissue sarcoma: a randomised phase 3 multicentre study. The Lancet Oncology. 2010;11(6):561-570.
3. Sapareto SA, Dewey WC. Thermal dose determination in cancer therapy. International Journal of Radiation Oncology*Biology*Physics. 1984;10(6):787-800.
4. Jaque D, Martínez Maestro L, del Rosal B, Haro-Gonzalez P, Benayas A, Plaza JL, et al. Nanoparticles for photothermal therapies. Nanoscale. 2014;6(16):9494-9530.
5. Khurshid H, Balakrishnan S, Colak L, Bonder MJ, Hadjipanayis GC. Water Dispersible Fe/Fe-Oxide Core-Shell Structured Nanoparticles for Potential Biomedical Applications. IEEE Transactions on Magnetics. 2009;45(10):4877-4879.
6. Pollert E, Kaspar P, Zaveta K, Herynek V, Burian M, Jendelova P. Magnetic Nanoparticles for Therapy and Diagnostics. IEEE Transactions on Magnetics. 2013;49(1):7-10.
7. Hergt R, Andra W, d'Ambly CG, Hilger I, Kaiser WA, Richter U, et al. Physical limits of hyperthermia using magnetite fine particles. IEEE Transactions on Magnetics. 1998;34(5):3745-3754.
8. Laurent S, Dutz S, Häfeli UO, Mahmoudi M. Magnetic fluid hyperthermia: Focus on superparamagnetic iron oxide nanoparticles. Advances in Colloid and Interface Science. 2011;166(1-2):8-23.
9. Lima E, Torres TE, Rossi LM, Rechenberg HR, Berquo TS, Ibarra A, et al. Size dependence of the magnetic relaxation and specific power absorption in iron oxide nanoparticles. Journal of Nanoparticle Research. 2013;15(5).
10. Barrera G, Coisson M, Celegato F, Raghuvanshi S, Mazaleyrat F, Kane SN, et al. Cation distribution effect on static and dynamic magnetic properties of Co1-xZnxFe2O4 ferrite powders. Journal of Magnetism and Magnetic Materials. 2018;456:372-380.
11. Hergt R, Dutz S, Müller R, Zeisberger M. Magnetic particle hyperthermia: nanoparticle magnetism and materials development for cancer therapy. J Phys: Condens Matter. 2006;18(38):S2919-S2934.
12. Branquinho LC, Carrião MS, Costa AS, Zufelato N, Sousa MH, Miotto R, et al. Effect of magnetic dipolar interactions on nanoparticle heating efficiency: Implications for cancer hyperthermia. Sci Rep. 2013;3(1).
13. Hergt R, Dutz S. Magnetic particle hyperthermia—biophysical limitations of a visionary tumour therapy. Journal of Magnetism and Magnetic Materials. 2007;311(1):187-192.
14. Brezovich IA, Meredith RF. Practical Aspects of Ferromagnetic Thermoseed Hyperthermia. Radiol Clin North Am. 1989;27(3):589-602.
15. Herrero de la Parte B, Rodrigo I, Gutiérrez-Basoa J, Iturrizaga Correcher S, Mar Medina C, Echevarría-Uraga JJ, et al. Proposal of New Safety Limits for In Vivo Experiments of Magnetic Hyperthermia Antitumor Therapy. Cancers (Basel). 2022;14(13):3084.
16. Ansari SR, Suárez-López YdC, Thersleff T, Häggström L, Ericsson T, Katsaros I, et al. Pharmaceutical Quality by Design Approach to Develop High-Performance Nanoparticles for Magnetic Hyperthermia. ACS Nano. 2024;18(23):15284-15302.
17. Kwok MKY, Maley CCJ, Dworkin A, Hattersley S, Southern P, Pankhurst QA. Nonspecific eddy current heating in magnetic field hyperthermia. Applied Physics Letters. 2023;122(24).
18. Hedayatnasab Z, Abnisa F, Daud WMAW. Review on magnetic nanoparticles for magnetic nanofluid hyperthermia application. Materials and Design. 2017;123:174-196.
19. Mehdaoui B, Meffre A, Carrey J, Lachaize S, Lacroix LM, Gougeon M, et al. Optimal Size of Nanoparticles for Magnetic Hyperthermia: A Combined Theoretical and Experimental Study. Adv Funct Mater. 2011;21(23):4573-4581.
20. Mohapatra J, Zeng F, Elkins K, Xing M, Ghimire M, Yoon S, et al. Size-dependent magnetic and inductive heating properties of Fe_3O_4 nanoparticles: scaling laws across the superparamagnetic size. Physical Chemistry Chemical Physics. 2018;20(18):12879-12887.
21. Nemati Z, Alonso J, Martinez LM, Khurshid H, Garaio E, Garcia JA, et al. Enhanced Magnetic Hyperthermia in Iron Oxide Nano-Octopods: Size and Anisotropy Effects. The Journal of Physical Chemistry C. 2016;120(15):8370-8379.
22. Lee J-H, Jang J-t, Choi J-s, Moon SH, Noh S-h, Kim J-w, et al. Exchange-coupled magnetic nanoparticles for efficient heat induction. Nature Nanotechnology. 2011;6(7):418-422.
23. Sugumaran PJ, Liu X-L, Herng TS, Peng E, Ding J. GO-Functionalized Large Magnetic Iron Oxide Nanoparticles with Enhanced Colloidal Stability and Hyperthermia Performance. ACS Applied Materials and Interfaces. 2019;11(25):22703-22713.
24. Du Y, Liu X, Liang Q, Liang X-J, Tian J. Optimization and Design of Magnetic Ferrite Nanoparticles with Uniform Tumor Distribution for Highly Sensitive MRI/MPI Performance and Improved Magnetic Hyperthermia Therapy. Nano Lett. 2019;19(6):3618-3626.
25. Liu X, Peng M, Li G, Miao Y, Luo H, Jing G, et al. Ultrasonication-Triggered Ubiquitous Assembly of Magnetic Janus Amphiphilic Nanoparticles in Cancer Theranostic Applications. Nano Lett. 2019;19(6):4118-4125.
26. Lv Y, Yang Y, Fang J, Zhang H, Peng E, Liu X, et al. Size dependent magnetic hyperthermia of octahedral Fe_3O_4 nanoparticles. RSC Advances. 2015;5(94):76764-76771.
27. Noh S-h, Na W, Jang J-t, Lee J-H, Lee EJ, Moon SH, et al. Nanoscale Magnetism Control via Surface and Exchange Anisotropy for Optimized Ferrimagnetic Hysteresis. Nano Lett. 2012;12(7):3716-3721.
28. Liu XL, Yang Y, Ng CT, Zhao LY, Zhang Y, Bay BH, et al. Magnetic Vortex Nanorings: A New Class of Hyperthermia

Agent for Highly Efficient In Vivo Regression of Tumors. Adv Mater. 2015;27(11):1939-1944.
29. Xiao W, Liu X, Hong X, Yang Y, Lv Y, Fang J, et al. Magnetic-field-assisted synthesis of magnetite nanoparticles via thermal decomposition and their hyperthermia properties. CrystEngComm. 2015;17(19):3652-3658.
30. Dutta B, Checker S, Barick KC, Salunke HG, Gota V, Hassan PA. Malic acid grafted Fe_3O_4 nanoparticles for controlled drug delivery and efficient heating source for hyperthermia therapy. Journal of Alloys and Compounds. 2021;883:160950.
31. Liu XL, Fan HM, Yi JB, Yang Y, Choo ESG, Xue JM, et al. Optimization of surface coating on Fe_3O_4 nanoparticles for high performance magnetic hyperthermia agents. Journal of Materials Chemistry. 2012;22(17):8235.
32. Vayssières L, Chanéac C, Tronc E, Jolivet JP. Size Tailoring of Magnetite Particles Formed by Aqueous Precipitation: An Example of Thermodynamic Stability of Nanometric Oxide Particles. Journal of Colloid and Interface Science. 1998;205(2):205-212.
33. Gnanaprakash G, Mahadevan S, Jayakumar T, Kalyanasundaram P, Philip J, Raj B. Effect of initial pH and temperature of iron salt solutions on formation of magnetite nanoparticles. Materials Chemistry and Physics. 2007;103(1):168-175.
34. Ramadan W, Kareem M, Hannoyer B, Saha S. Effect of pH on the Structural and Magnetic Properties of Magnetite Nanoparticles Synthesised by Co-Precipitation. Advanced Materials Research. 2011;324:129-132.
35. Myrovali E, Papadopoulos K, Charalampous G, Kesapidou P, Vourlias G, Kehagias T, et al. Toward the Separation of Different Heating Mechanisms in Magnetic Particle Hyperthermia. ACS Omega. 2023;8(14):12955-12967.
36. Dheyab MA, Aziz AA, Jameel MS, Noqta OA, Khaniabadi PM, Mehrdel B. Simple rapid stabilization method through citric acid modification for magnetite nanoparticles. Sci Rep. 2020;10(1).
37. Sureshkumar V, Kiruba Daniel SCG, Ruckmani K, Sivakumar M. Fabrication of chitosan–magnetite nanocomposite strip for chromium removal. Applied Nanoscience. 2015;6(2):277-285.
38. Jubb AM, Allen HC. Vibrational Spectroscopic Characterization of Hematite, Maghemite, and Magnetite Thin Films Produced by Vapor Deposition. ACS Applied Materials and Interfaces. 2010;2(10):2804-2812.
39. Pathak S, Verma R, Kumar P, Singh A, Singhal S, Sharma P, et al. Facile Synthesis, Static, and Dynamic Magnetic Characteristics of Varying Size Double-Surfactant-Coated Mesoscopic Magnetic Nanoparticles Dispersed Stable Aqueous Magnetic Fluids. Nanomaterials. 2021;11(11):3009.
40. Samanifar S, Alikhani M, Almasi Kashi M, Ramazani A, Montazer AH. Magnetic alloy nanowire arrays with different lengths: Insights into the crossover angle of magnetization reversal process. Journal of Magnetism and Magnetic Materials. 2017;430:6-15.
41. Guardia P, Di Corato R, Lartigue L, Wilhelm C, Espinosa A, Garcia-Hernandez M, et al. Water-Soluble Iron Oxide Nanocubes with High Values of Specific Absorption Rate for Cancer Cell Hyperthermia Treatment. ACS Nano. 2012;6(4):3080-3091.
42. Ge J, Hu Y, Biasini M, Beyermann WP, Yin Y. Superparamagnetic Magnetite Colloidal Nanocrystal Clusters. Angew Chem Int Ed. 2007;46(23):4342-4345.
43. Lu A-H, Salabas EL, Schüth F. Magnetic Nanoparticles: Synthesis, Protection, Functionalization, and Application. Angew Chem Int Ed. 2007;46(8):1222-1244.
44. Jordan A, Wust P, Scholz R, Tesche B, Fähling H, Mitrovics T, et al. Cellular uptake of magnetic fluid particles and their effects on human adenocarcinoma cells exposed to AC magnetic fields in vitro. International Journal of Hyperthermia. 1996;12(6):705-722.
45. Li Z, Kawashita M, Araki N, Mitsumori M, Hiraoka M, Doi M. Magnetite nanoparticles with high heating efficiencies for application in the hyperthermia of cancer. Materials Science and Engineering: C. 2010;30(7):990-996.
46. Linfeng C, Ong CK, Tan BTG. Study of electrical transport properties of fine magnetic particles using microwave Hall effect techniques. IEEE Transactions on Magnetics. 1998;34(1):272-277.
47. Ruta S, Hovorka O, Huang P-W, Wang K, Ju G, Chantrell R. First order reversal curves and intrinsic parameter determination for magnetic materials; limitations of hysteron-based approaches in correlated systems. Sci Rep. 2017;7(1).
48. Roberts AP, Pike CR, Verosub KL. First-order reversal curve diagrams: A new tool for characterizing the magnetic properties of natural samples. Journal of Geophysical Research: Solid Earth. 2000;105(B12):28461-28475.
49. Muxworthy AR, Dunlop DJ. First-order reversal curve (FORC) diagrams for pseudo-single-domain magnetites at high temperature. Earth and Planetary Science Letters. 2002;203(1):369-382.
50. Périgo EA, Hemery G, Sandre O, Ortega D, Garaio E, Plazaola F, et al. Fundamentals and advances in magnetic hyperthermia. Applied Physics Reviews. 2015;2(4):041302.
51. Oliveira TR, Stauffer PR, Lee C-T, Landon CD, Etienne W, Ashcraft KA, et al. Magnetic fluid hyperthermia for bladder cancer: A preclinical dosimetry study. International Journal of Hyperthermia. 2013;29(8):835-844.
52. Alphandéry E, Faure S, Raison L, Duguet E, Howse PA, Bazylinski DA. Heat Production by Bacterial Magnetosomes Exposed to an Oscillating Magnetic Field. The Journal of Physical Chemistry C. 2010;115(1):18-22.
53. Soetaert F, Kandala SK, Bakuzis A, Ivkov R. Experimental estimation and analysis of variance of the measured loss power of magnetic nanoparticles. Sci Rep. 2017;7(1).
54. Figuerola A, Di Corato R, Manna L, Pellegrino T. From iron oxide nanoparticles towards advanced iron-based inorganic materials designed for biomedical applications. Pharmacol Res. 2010;62(2):126-143.
55. Glöckl G, Hergt R, Zeisberger M, Dutz S, Nagel S, Weitschies W. The effect of field parameters, nanoparticle properties and immobilization on the specific heating power in magnetic particle hyperthermia. J Phys: Condens Matter. 2006;18(38):S2935-S2949.
56. Muro-Cruces J, Roca AG, López-Ortega A, Fantechi E, del-Pozo-Bueno D, Estradé S, et al. Precise Size Control of the Growth of Fe_3O_4 Nanocubes over a Wide Size Range Using a Rationally Designed One-Pot Synthesis. ACS Nano. 2019;13(7):7716-7728.
57. Obaidat I, Issa B, Haik Y. Magnetic Properties of Magnetic Nanoparticles for Efficient Hyperthermia. Nanomaterials. 2015;5(1):63-89.